Effects of grain boundary chemistry and precipitate structure on intergranular corrosion in Al-Mg-Si alloys doped with Cu and Zn

Bartawi, Emad H.; Marioara, Calin D.; Shaban, Ghada; Rahimi, Ehsan; Mishin, Oleg V.; Sunde, Jonas K.; Gonzalez-Garcia, Yaiza; Holmestad, Randi; Ambat, Rajan

DOI
10.1016/j.corsci.2024.112227

Publication date
2024

Document Version
Final published version

Published in
Corrosion Science

Citation (APA)
Bartawi, E. H., Marioara, C. D., Shaban, G., Rahimi, E., Mishin, O. V., Sunde, J. K., Gonzalez-Garcia, Y., Holmestad, R., & Ambat, R. (2024). Effects of grain boundary chemistry and precipitate structure on intergranular corrosion in Al-Mg-Si alloys doped with Cu and Zn. *Corrosion Science*, *236*, Article 112227. https://doi.org/10.1016/j.corsci.2024.112227

Corrosion Science 236 (2024) 112227

Contents lists available at ScienceDirect

Corrosion Science

journal homepage: www.elsevier.com/locate/corsci

Effects of grain boundary chemistry and precipitate structure on intergranular corrosion in Al-Mg-Si alloys doped with Cu and Zn

Emad H. Bartawi [a,*], Calin D. Marioara [b], Ghada Shaban [a], Ehsan Rahimi [c], Oleg V. Mishin [a], Jonas K. Sunde [d], Yaiza Gonzalez-Garcia [c], Randi Holmestad [e], Rajan Ambat [a]

[a] Department of Civil and Mechanical Engineering, Technical University of Denmark, Kgs. Lyngby 2800, Denmark
[b] Materials and Nanotechnology, SINTEF Industry, Trondheim N-7465, Norway
[c] Department of Materials Science and Engineering, Delft University of Technology, Mekelweg 2, Delft 2628 CD, the Netherlands
[d] Hydro Extrusions, Innovation & Technology Precision Tubing, Drammensveien 264, Oslo 0283, Norway
[e] Department of Physics, NTNU, Norwegian University of Science and Technology, Trondheim 7491, Norway

ARTICLE INFO

Keywords:
Recycled Al-Mg-Si alloys
Intergranular corrosion
Precipitate atomic structures
HR-STEM
AFM/SKPFM

ABSTRACT

Al-Mg-Si alloys are known as structural materials and are primary alloys in the automotive industry to achieve weight reduction. Shifting toward sustainability, lower energy consumption, and less CO_2 emission necessitates recycling. However, the unavoidable accumulation of scrap-related impurities, e.g., Cu and Zn, during the recycling process can influence corrosion resistance of recycled alloys. The results show that Al-Mg-Si alloys containing 0.05 wt% Cu exhibit low intergranular corrosion resistance. The intergranular corrosion resistance of these alloys is notably improved by adding 0.06 wt% Zn. Low concentrations of Cu and Zn are found to strongly affect the crystal structure of hardening precipitates.

1. Introduction

Al-Mg-Si (6xxx series) extrusions are widely used in marine, architecture, aerospace, and automotive applications, owing to their good formability, high strength-to-weight ratio, excellent recycling potential, and good corrosion resistance [1,2]. The demand for Al-Mg-Si alloys in the automotive sector is rising, driven by increased production of lightweight electrical vehicles. Therefore, intensive studies on the processing technology, mechanical and electrical properties, and alloy design for the 6xxx-series Al alloys have been performed [3–6]. Despite the good corrosion resistance of the Al-Mg-Si alloys, various issues linked to localized corrosion attacks can occur as a result of inadequate heat treatments or due to the presence of Zn or Cu [7–9]. It has also been reported that the misorientation angle and local plastic deformation introduced during alloy manufacturing can noticeably influence the intergranular corrosion (IGC) resistance [10–12]. The IGC in these alloys is associated with a micro-galvanic coupling between anodic and cathodic electrochemically active sites at grain boundaries (GBs) in the microstructure.

In Al-Mg-Si alloys with additions of Cu, it is believed that the IGC occurs as a result of differences in the electrochemical potential between the anodic sites (precipitate-free zones (PFZ) and the Al matrix) and the cathodic sites (Cu-rich films and Cu-containing particles such as Q/Q′) [11,13–16]. The susceptibility to IGC corrosion is not only related to the chemical composition, but also to aging conditions, which play a considerable role in determining the IGC resistance in the Al-Mg-Si alloys [15,17–19]. For instance, Svenningsen et al. [15] reported that an Al-Mg-Si alloy with 0.12 wt% Cu demonstrated increased susceptibility to IGC and that IGC in this alloy was affected by the thermal history. The alloy subjected to quenching at a higher rate exhibited higher resistance to IGC compared to the alloy quenched at a lower rate. The IGC susceptibility of Cu-containing Al-Mg-Si alloys has been mainly ascribed to the presence of Cu-rich films and/or Q/Q′ particles formed along GBs. It is usually claimed that IGC can be limited by keeping the Cu level below 0.1 wt% [15,20,21]—. However, some recent work has shown that IGC can be affected even by smaller amounts of Cu (0.05–0.06 wt%) [10,22]. The results in Ref. [10] showed the presence of Q/Q′ particles and Cu-rich films along some random high angle GBs with PFZs formed around such boundaries. Moreover, β particles and PFZs were also observed along coincidence site lattice GBs. Closely spaced Q/Q′ and β particles were observed along some low angle boundaries with no well-developed PFZs [10].

* Corresponding author.
E-mail address: ehaba@mek.dtu.dk (E.H. Bartawi).

https://doi.org/10.1016/j.corsci.2024.112227
Received 21 February 2024; Received in revised form 15 May 2024; Accepted 21 June 2024
Available online 24 June 2024

The Mg/Si ratio, concentrations of Zn and Cu, and heat treatments noticeably influence the types, frequency and sizes of particles in Al-Mg-Si alloys [13,23–25]. The precipitation process from supersaturated solid solution (SSSS) in Cu-free Al-Mg-Si alloys is usually described by the following sequence [26]:

SSSS → clusters→ GP-zones→ β″→ β′, U1, U2, B′→ β+Si

A more complex precipitation sequence is reported in Cu-containing Al-Mg-Si alloys, where Cu is added to increase the number density of fine precipitates and hence strength [27–32]. Furthermore, additions of Cu cause significant changes in the compositions of clusters and precipitates [13,33–35]. The precipitation sequence in the presence of relatively high copper concentrations is described as [27,30,31]:

SSSS → clusters→ GP-zones→ β″, L → β'_{Cu}, S, Q′, C → Q + Si

In the past several years, the effect of Zn additions on the precipitation and mechanical properties of Al-Mg-Si alloys attracted significant attention because Zn in relatively high concentrations can result in significant hardening [36–40]. For example, Ding et al. investigated age-hardening response in two Al-Mg-Si alloys with either 0.5 wt% or 3 wt% Zn [38]. The results showed a considerable increase in age hardening after adding 3 wt% Zn compared to the effect of 0.5 wt% Zn. The observed increase in hardness was linked to the presence of different types of precipitates, β-Mg_2Si and η-$MgZn_2$, after aging at 200 °C for 24 h. The same observation was made by Guo et al. [39], who reported that the addition of 1 wt% Zn enhanced the hardening response in aged Al-0.82Mg-0.91Si alloys. Studies of the influence of Zn addition on precipitate structures were conducted by Saito et al. [7,41]. Their results exhibited that Zn had a weak preference for occupancy of specific atomic sites in Al-Mg-Si precipitates. No measurable effect on the precipitate structure was detected in the alloys containing up to 0.1 wt% Zn. A minor addition of Zn (≤ 0.1 wt%) was found to have negligible influence on the IGC resistance [7]. However, strong evidence of IGC was observed in an alloy containing 1 wt% Zn. The influence of Zn additions on the IGC of two Al-Mg-Si alloys was investigated by Chi et al. [42], who demonstrated that the IGC penetration depth was greater in an alloy with 0.2 wt% Zn than in an alloy with 0.05 wt% Zn. In general, Zn additions were found to result in a higher number density of GB particles and wider PFZs, resulting in more susceptibility to IGC. Nevertheless, particularly high IGC resistance in an Al-Mg-Si-0.2Cu alloy containing 0.1 wt% Zn was documented by Yamaguchi et al. [43] after a baking heat treatment, while alloys with higher than 0.1 wt% Zn (up to 0.48 wt %) showed low IGC resistance.

The effect of low Zn content (≤ 0.06 wt%) in combination with a low concentration of Cu on the microstructure and IGC in Al-Mg-Si alloys have not been previously studied. Currently, Cu and Zn are practically unavoidable in recycled Al-Mg-Si alloys and, therefore, expected to be present in low concentrations in many 6xxx-series alloys with high levels of recycled Al content. Therefore, it is essential to evaluate how low concentrations of scrap-related Cu and Zn will influence the microstructure and IGC resistance of these alloys. This evaluation is the main goal of the present study. Results of this study will help to determine appropriate proportions of Al scrap and virgin aluminum in final products without sacrificing their corrosion resistance. In addition, the present work intends to provide detailed information on the influence of 0.05 wt% Cu combined with a varying concentration of Zn (≤0.06 wt%) on the precipitate structure in aged Al-Mg-Si alloys as their structure in the presence of Cu and Zn is still not fully understood. Furthermore, possible ways of enhancing the resistance to IGC in Al-Mg-Si alloys containing small Cu concentrations are proposed. To characterize grain structures, precipitates and IGC, a variety of electron microscopy techniques have been used in this work. These include high-angle annular dark-field scanning transmission electron microscopy (HAADF-STEM), scanning electron microscopy (SEM) and electron backscatter diffraction (EBSD). In addition, atom force microscopy (AFM) coupled with scanning Kelvin probe force microscopy (SKPFM) is utilized to evaluate the surface potential difference between the matrix and GBs containing Cu and Zn as films.

2. Experimental methods

2.1. Material used

The chemical compositions of four Al-Mg-Si alloys used in the present work are given in Table 1. The main difference between these alloys was in the amount of Zn, 0.003, 0.02, 0.04, and 0.06 wt% for samples A1, A2, A3 and A4, respectively. The alloy compositions were achieved by gradually increasing the concentrations of specific elements in one base Al-Mg-Si alloy. At first, Cu was added to the alloy, followed by a gradual increase in Zn content to achieve the desired concentrations. To verify the actual composition of the alloys, Optical Emission Spectrometry (OES) analysis was performed after casting. Despite the varying composition, all the samples are within the standard range for the AA6082 alloy.

As-cast ingots were homogenized at 575 °C for 135 min. Thereafter, the ingots were extruded at a ram speed of 5.6 mm/s and at an average temperature of 530 °C into flat profiles with a thickness of 4 mm. The extruded profiles were water quenched, stretched 0.5 % and subjected to a two-step aging process to obtain a peak-aged condition. Hydro Aluminium designates this condition as temper T6.

2.2. Microstructure characterization

The initial microstructural characterization was performed using light optical microscopy to observe the microstructure in three orthogonal planes. Several 25 × 10 × 4 mm^3 specimens were at first mechanically ground and then polished using a polishing suspension with a diamond size of 1 μm. Thereafter, the specimens were etched using the tetrafluoroboric acid, and optical micrographs were obtained using a Zeiss Axio Vert.A1 microscope from three orthogonal planes: (i) the longitudinal section containing the extrusion direction (ED) and the normal direction (ND); (ii) the cross-section containing the transverse direction (TD) and the ND, and (iii) the surface containing the ED and TD.

—The EBSD analysis of the as-received microstructure was conducted both in the ED-TD plane and in the ED-ND plane. For examinations of the ED-TD plane, the top surface of the extruded material was mechanically polished and then electropolished to obtain good-quality EBSD patterns. The thickness of the surface layer removed by polishing was estimated to be 40–50 μm. EBSD data in this plane were collected in several regions, covering a total area of 2 mm^2 with a step size of 1 μm. The ED-ND plane was investigated by EBSD in samples A1 and A4. After polishing, EBSD data were obtained in these samples covering an area of ~1.3 mm^2 with a step size of 2 μm.

Specimens for transmission electron microscopy (TEM) were ground to approximately 100 μm thickness and punched into 3 mm discs. The discs were then electropolished in a solution of 800 ml ethanol, 100 ml 2-butoxyethanol and 100 ml perchloric acid (65 %) at approximately −25 °C. TEM investigations of GBs were conducted using a Titan analytical 80–300ST microscope operated at 300 kV and equipped with an energy dispersive spectroscopy (EDS) detector X-Max 80TLE. A

Table 1
Chemical composition (wt%) of the four Al-Mg-Si samples used in the present study.

Sample	Cu	Mg	Si	Fe	Zn	Mn	Al
A1	0.048	0.647	0.968	0.219	0.003	0.544	Balance
A2	0.050	0.628	0.937	0.211	0.022	0.554	Balance
A3	0.050	0.636	0.942	0.216	0.041	0.562	Balance
A4	0.050	0.627	0.949	0.208	0.059	0.580	Balance

double-corrected JEOL ARM200CF microscope operated at 200 kV was employed to obtain high resolution Z-contrast HAADF-STEM images of fine precipitates in grain interiors. Since these precipitates were produced by growth along ⟨001⟩ directions in the matrix, HAADF-STEM images were taken after tilting the foil to a [001] zone axis, which enabled viewing the precipitates in their cross-sections. The images were taken using a probe size of 0.10 nm and a convergence semi-angle of ~27 mrad. The inner and outer collection angles of the HAADF detector were 51 and 203 mrad, respectively. To reduce scanning noise, fast Fourier transform (FFT) filtering was applied for all images using a circular band pass mask to remove all periods shorter than approximately 0.15 nm, which was close to the shortest separation of projected atomic columns in precipitates viewed in the cross-section.

2.3. Hardness measurements

Vickers hardness was measured in each as-received alloy using a load of 500 g and a dwell time of 15 s. Prior to hardness measurements the surface was mechanically polished using the same polishing suspension as the one applied for sample preparation for optical microscopy.

2.4. AFM/SKPFM analysis

To reveal the impact of the minor additions of Cu and Zn on the difference in surface potential between GBs and grain interiors, AFM and SKPFM surface-sensitive analysis was performed using a Bruker Dimension Edge™ instrument with an n-type doped silicon pyramid single crystal tip coated with a PtIr5 (SCM-Pit probe) having a height of 10–15 μm and a tip radius of 20 nm. Prior to AFM and SKPFM, specimens were polished using oxide polishing suspensions with a final grain size of 0.25 μm. The polished surface was then marked by focused ion Xe beam. The local surface potential was recorded in the dual-scan mode. At first, topography maps were recorded in the tapping mode, after which the tip was lifted to 100 nm and the surface potential was recorded by following the topography contour registered in the first scan. The topography and surface potential images were captured in air at 22 °C and at a relative humidity of approximately 32 %. The pixel resolution was 512 × 512 and the scan frequency rate was 0.3 Hz. In addition, zero-bias voltage and tip bias were adopted in all the experiments.

2.5. Intergranular corrosion tests

The influence of trace level Zn content on the microstructure and IGC of the prepared alloys was investigated using 25 × 20 × 4 mm^3 specimens, which were alkaline etched at 56 °C for 5 min in a solution containing 8 % NaOH and then immersed in nitric acid for 2 min, rinsed in distilled water and dried in a cooled air stream. The thickness of the removed surface layer due to etching was estimated to be ~15 μm [22,44]. IGC tests were performed by exposing the prepared specimens to an acidified salt solution containing 10 ml/l of concentrated HCl and 30 g/l NaCl at room temperature for 24 h. The IGC test was performed according to the BS ISO 11846 (method B) standard [45]. The studied extrusions had a recrystallized surface layer and a largely non-recrystallized microstructure in the interior layer. In the present work, analysis was focused on the recrystallized surface layer as this was the layer exposed to the corrosive environment. Lacomit varnish was used to protect the specimen sides, so that only the ED-TD surface would be exposed to the acidified solution during the IGC test. After the immersion test, the specimens were rinsed in distilled water and then air-dried. Analysis of IGC was performed both on the corroded surface and in the ED-ND section. The exposed surface and the mechanically polished ED-ND section were investigated after the test in an AFEG 250 analytical environmental SEM.

3. Results

3.1. Optical microscopy and SEM/EBSD observations

The four studied extrusions have 0.4–0.5-mm-thick recrystallized layers at the top and bottom surfaces and a largely non-recrystallized ~3-mm-thick interior layer (Fig. 1). The grain size in the recrystallized layer of each sample varies as a function of depth; the average size of grains close to the top surface is 20-30 μm, while grains with sizes of several hundred micrometers and up to the millimeter range are observed near the non-recrystallized layer.

At depths of 40–50 μm investigated using EBSD, the average grain sizes are 63 μm in sample A1 and 40 μm in sample A4, see Fig. 2a,b. To verify that the difference in the average grain size is not caused by the small differences in depths at which the orientation maps were collected, additional maps from the ED-ND section were obtained (see Fig. 2c,d). These maps indicate that within the first 50 μm below the immediate surface there are indeed many more fine grains in sample A4 than sample A1. Despite the difference in the average grain sizes, fractions of low angle boundaries f_{LAB}, measured at 40–50 μm below the surface, are almost identical (9–10 %) in these samples. Crystallographic textures in each sample are weak, with slightly increased fractions of the Goss {110}⟨001⟩ and shear {001}⟨110⟩ components (see Table 2). SEM examination (not shown here) reveals the presence of comparatively coarse intermetallic particles (IMPs), mostly identified as the Al(MnFe)Si phase though some of them also contain Cu.

The results of hardness measurements are shown in Fig. 3. It is seen that the hardness decreases very slightly (from ~112 HV to ~110 HV) as the Zn content increases from 0.003 wt% in sample A1 to 0.06 wt% in sample A4.

3.2. Results of TEM and STEM analysis

Bright-field TEM images show that GBs contain rather coarse particles (Fig. 4). Regions adjacent to the GBs demonstrate PFZs with a width of ~100 nm, while grain interiors contain fine needle- and rod-shaped precipitates. No apparent differences in sizes and number densities of these precipitates are observed between the different samples. To obtain more detailed information about the microstructure in the GB regions, thin foils from sample A1 with the lowest Zn content and from sample A4 with the highest Zn content were additionally investigated using STEM and EDS.

Fig. 5a,c shows HAADF-STEM images of two GBs in sample A1, which are aligned almost parallel to the electron beam. Results of the EDS analysis reveal the presence of continuous Cu-rich films along some GBs. Such Cu-rich films were observed along seven boundaries out of sixteen GBs analyzed in sample A1. The films were observed both along GBs free of particles and along GBs with particles, see Fig. 5 and Fig. S1. The GB particle in the center of Fig. 5a is identified as the Q/Q′ phase containing Mg, Si, and Cu [11,46]. In addition, β particles are also observed along some GBs in sample A1 (see Figure S2).

Similar to sample A1, sample A4 exhibits PFZs along the inspected grain boundaries. The majority of investigated boundaries in sample A4 contain either only Cu-rich films or no observable films at all. However, in several cases, continuous GB films enriched in both Cu and Zn are also observed in this sample (Fig. 6). The concentration of Cu within such films is significantly higher than that of Zn. Interestingly, Zn-depleted zones are revealed within ~20 nm on each side of the boundary having the Cu/Zn film, i.e. the total width of such zones is ~40 nm (see Fig. 6d). The EDS maps in Fig. 6 show that the grain boundaries contain two types of precipitates identified as Q/Q′ particles and Zn-containing Q/Q′ particles.

All the atomic resolution HAADF-STEM images shown in this work were taken from sample A1 (with 0.05 wt% Cu) and sample A4 (with 0.05 wt% Cu and 0.06 wt% Zn). Since the precipitates in the studied alloys grow along ⟨100⟩ Al directions, the Al matrix was aligned along a

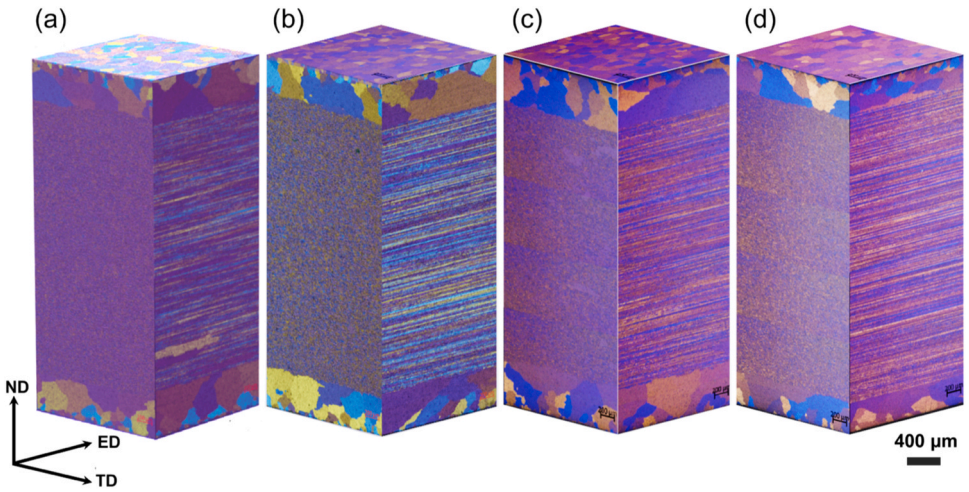

Fig. 1. Optical micrographs showing the microstructure of extruded samples in three orthogonal planes: (a) sample A1; (b) sample A2; (c) sample A3; (d) sample A4.

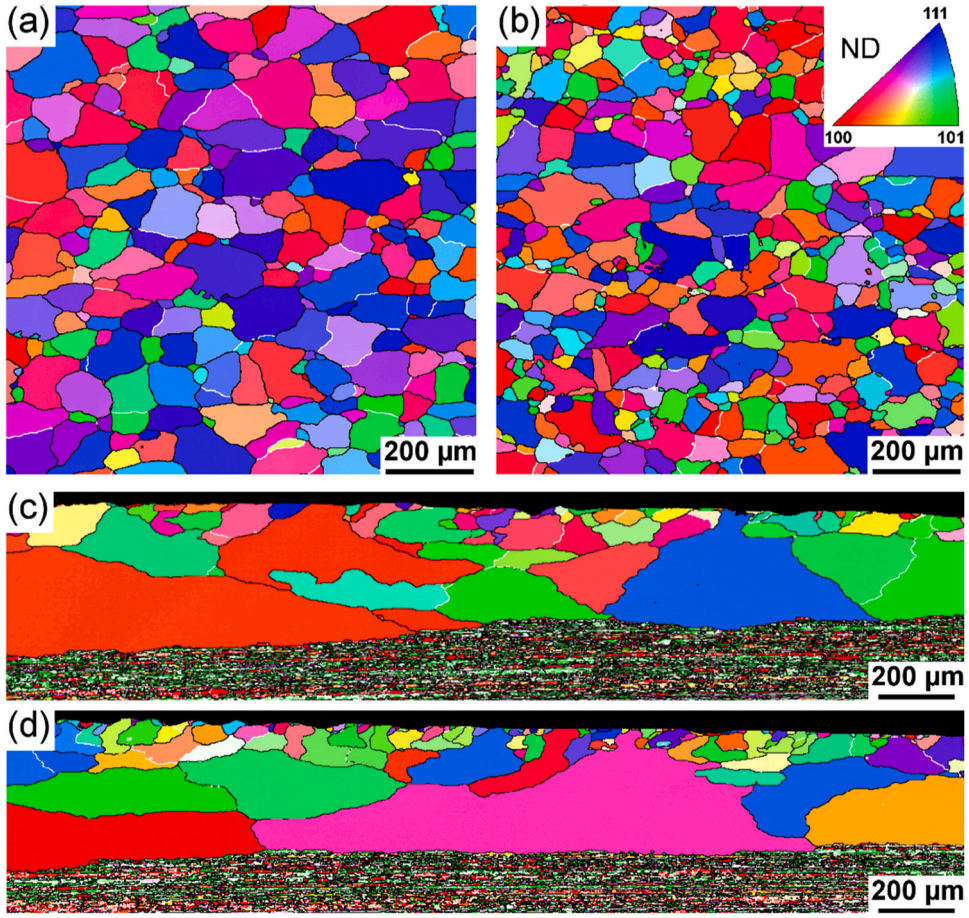

Fig. 2. Orientation maps obtained from the subsurface layer of samples A1 (a,c) and A4 (b,d): (a,b) ED-TD plane at 40–50 μm below the immediate surface; (c,d) ED-ND section. White and black lines in (a,b) correspond to LABs and HABs, respectively.

Table 2
Characteristics of the microstructure and texture in samples A1 and A4 analyzed using EBSD in the recrystallized layer at a depth of 40–50 μm.

Sample	Average grain size (μm)	f_{LAB} (%)	Fractions of texture components (%)				
			G {110}⟨001⟩	Bs {110}⟨112⟩	S {123}⟨634⟩	Cu {112}⟨111⟩	Shear {001}⟨110⟩
A1	63	9	6	1	5	2	7
A4	40	10	9	1	3	4	10

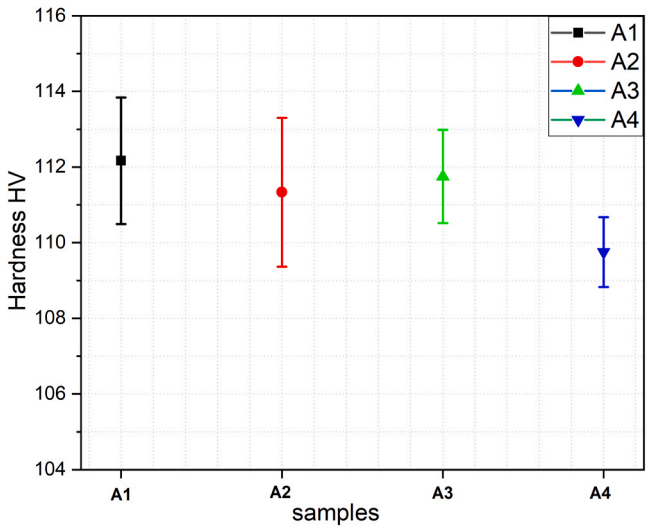

Fig. 3. Vickers hardness data for samples A1, A2, A3, and A4.

[001] Al zone axis, which enables imaging of precipitate cross-sections. The images were FFT-filtered as described in section 2.2, and atomic columns were overlaid, thus solving the precipitate atomic structures. The overlay was based on the solved crystal structures of different metastable phases in the Al-Mg-Si(-Cu) system [25,31,47–51] and the construction rules of such precipitates from Ref. [52] combined with Z-contrast information. According to the construction rules, every Al atom in the overlay is surrounded by 4 atoms found in different planes, every Mg is surrounded by 5 atoms, and every Si is surrounded by 3 atoms (making a triangular site). Cu in the Q/Q′ and C-phase unit cells also form a triangular site, while Cu atoms located at the precipitate/matrix incoherent interface can be surrounded by 4 atoms. In sample A4, the bright columns that do not relate to the known Cu configurations are assumed to be partly occupied by Zn.

Examples of the most common precipitate crystal structures in samples A1 and A4 are shown in Figs. 7 and 8, respectively. The shown precipitates can be considered representative of each sample as they were chosen from a series of images. The HAADF-STEM images in Fig. 7 acquired from sample A1 demonstrate β″ and fragmented β″ precipitates, which are the main hardening precipitates in the AA6082 alloy. Here fragmented β″ precipitates (Fig. 7c) are defined as those containing at least one unit configuration different from the β″ structural unit. Almost all precipitates in sample A1 show some columns with a higher intensity than other equivalent columns due to partial occupancy by Cu. Interestingly, 0.05 wt% Cu affects the precipitates noticeably and unexpectedly, considering both the concentration and aging condition. Q′/C configurations are observed in the β″ precipitate crystal structures, leading to an alteration of their structure, as seen in Fig. 7c. Precipitates in sample A4 exhibited noticeable differences in their crystal structures as more disordered structures were noticed compared to those in sample A1, as shown in Fig. 8a,d. Moreover, brighter columns inside the β″ structure, namely Si_3/Al, Si_1, and Si_2 sites are observed (Fig. 8c).

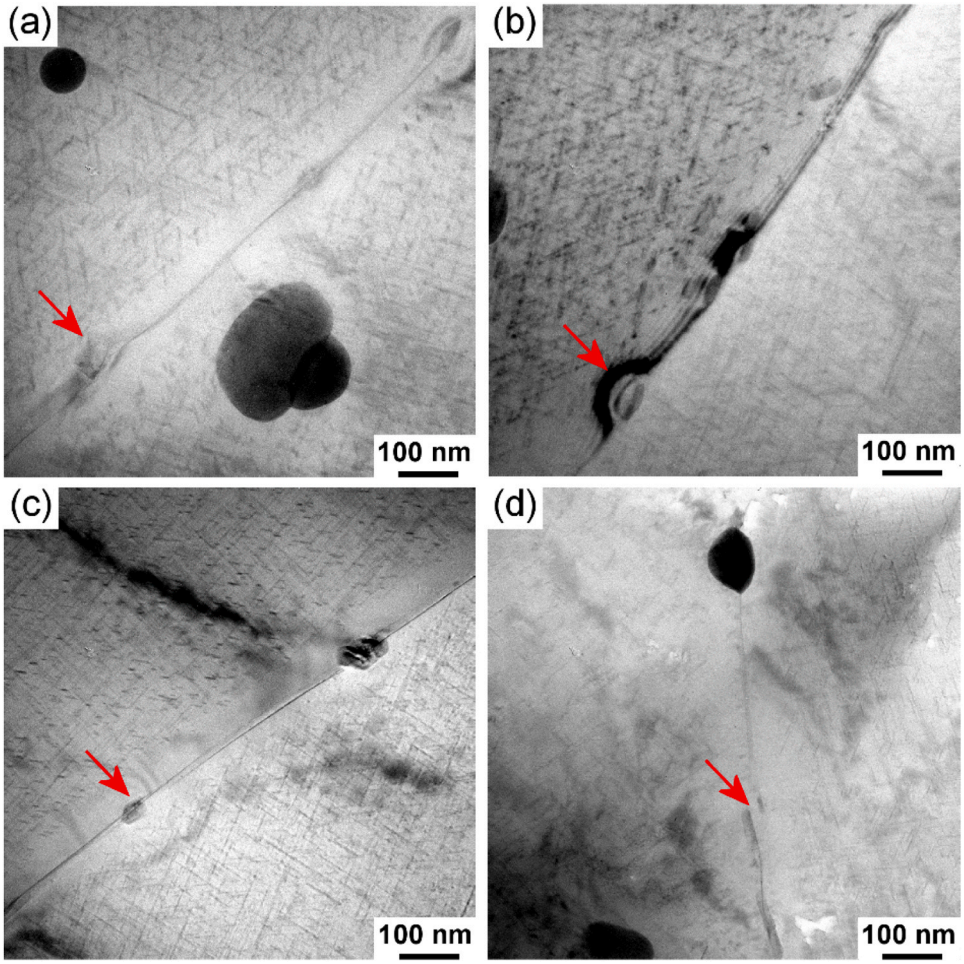

Fig. 4. Bright-field TEM images showing the microstructure in GB regions of the different samples: (a) sample A1; (b) sample A2; (c) sample A3; (d) sample A4. Red arrows show some examples of GB particles.

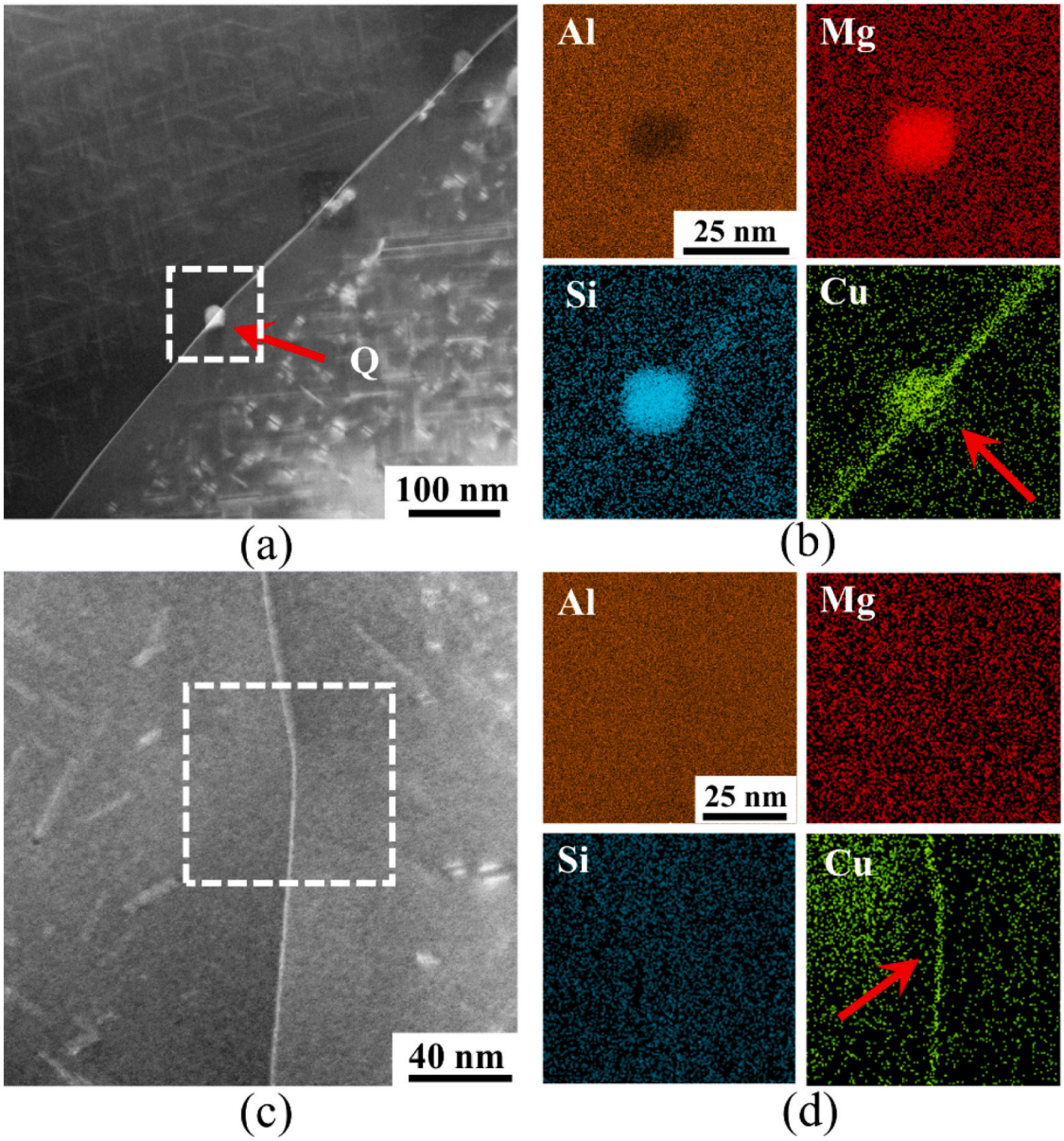

Fig. 5. HAADF-STEM images (a,c) from GB regions in sample A1 and EDS maps (b,d) showing distributions of different elements in the framed areas in (a,c). The arrow in (a) shows a Q/Q′ particle. The arrows in (b,d) indicate increased concentrations of Cu forming Cu-rich films along the GBs.

3.3. AFM/SKPFM characterization of GB regions

The segregation of Cu and Zn along the GBs forming Cu/Cu+Zn rich films with different work function energies (WFE) and surface potentials than those for the matrix can act as sites for nanoscale coupling. To measure the electrical surface potential and the difference in the surface charge between GBs and their adjacent areas, AFM coupled with SKPFM was conducted for sample A4 containing similar concentrations of Cu and Zn. Fig. 9a,b display low-magnification images of surface topography and surface potentials at a GB alongside large intermetallic particles (the dark color circles in Fig. 9b). From the topography image in Fig. 9a, it can be concluded that the intermetallic particles are not easily recognizable, which further confirms an appropriate surface preparation and especially the lowest impact of surface topography on the surface potential. It is discernible that all large IMPs represent the lowest surface potential with different values than the matrix (~30–80 mV) due to slight variations in the local distribution of chemical elements including the presence of oxide film. To better ascertain the local surface potential and/or surface charge at the GB, AFM/SKPFM analysis of the GB region was conducted at a high magnification, as presented in Fig. 9c,d. The SEM image in Fig. 9e shows the presence of two different grains and the GB corresponding to the AFM/SKPFM images, see Fig. 9c,d. It is seen that near the GB, the average surface potential drops by ~5 mV compared to values in the matrix. The region of the lower surface potential is indicated by vertical lines in Fig. 9g. The width of this region is ~100 nm, which corresponds to the width of PFZs observed in the TEM images, see Fig. 6.

3.4. Evaluation of intergranular corrosion

To investigate the effect of Zn on IGC resistance in the presence of 0.05 wt% Cu, the accelerated corrosion test was performed. The obtained SEM images of the surface subjected to IGC tests are shown in Fig. 10. It is evident that sample A1 with the lowest (0.003 wt%) Zn content is heavily affected by IGC. In this sample, there is a high frequency of corroded boundaries (seen as dark lines in Fig. 10a,e) and a large number of cavities formed by grains fallen out during the IGCs test. With increasing Zn content, the frequencies of corroded GBs and cavities

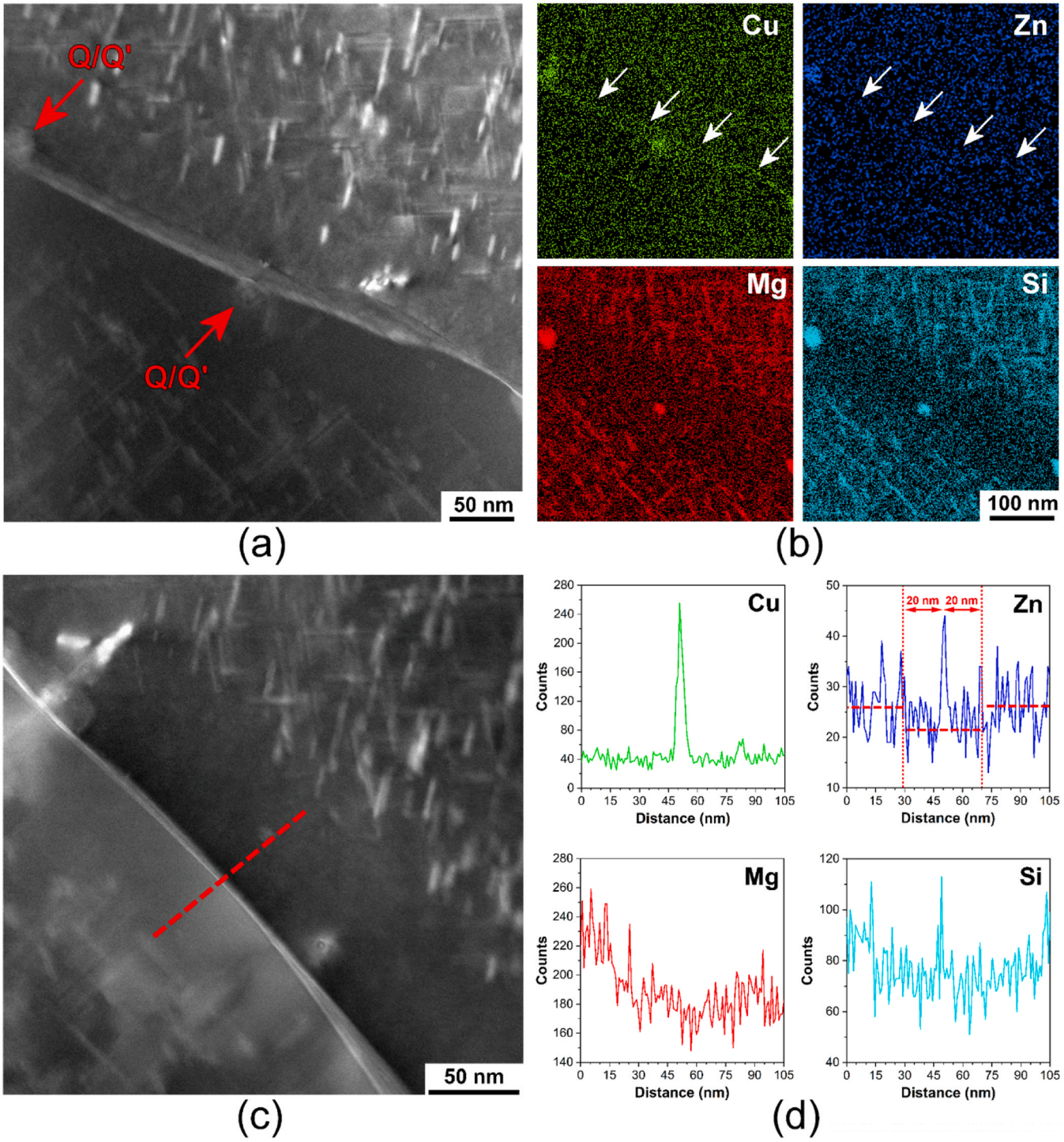

Fig. 6. GB regions in sample A4 analyzed using STEM: (a, c) HAADF-STEM images; (b) elemental maps obtained by EDS for the region shown in (a); (d) distribution of elements along the dashed line in (c). Arrows in (a) indicate two Q/Q′ particles, while arrows in (b) indicate a film enriched in Cu and Zn. Note that one of the Q/Q′ particles seen in (a, b) contains an increased concentration of both Cu and Zn, while no increased concentration of Zn is seen for the second particle. The horizontal red lines in the Zn map in (d) represent average Zn concentrations in the PFZ within approximately 20 nm on each side from the GB.

decrease. The lowest frequencies of corroded boundaries and cavities are observed in sample A4 with 0.06 wt% Zn.

Following our previous work [22], the extent of IGC is quantified here based on a new parameter defined as the number of corroded boundaries observed in the SEM image per unit area (N_C). Fig. 11a shows that N_C decreases from 258 mm^{-2} in sample A1 to 142 mm^{-2} in sample A4. The maximum penetration depth of IGC (Z_C) is also sensitive to the Zn content, as is seen in SEM images from polished ED-ND sections of the specimens subjected to the IGC tests (see Figure S3). Fig. 11b shows that the largest $Z_C = 260$ μm is recorded in sample A1 and that Z_C decreases with increasing Zn content. This observation indicates that Zn addition plays a significant role in defining IGC resistance in Al-Mg-Si alloys with low levels of Cu. This is in line with the images shown in Fig. 10, which demonstrate fewer corroded GBs in sample A4 than in samples A1, A2 and A3.

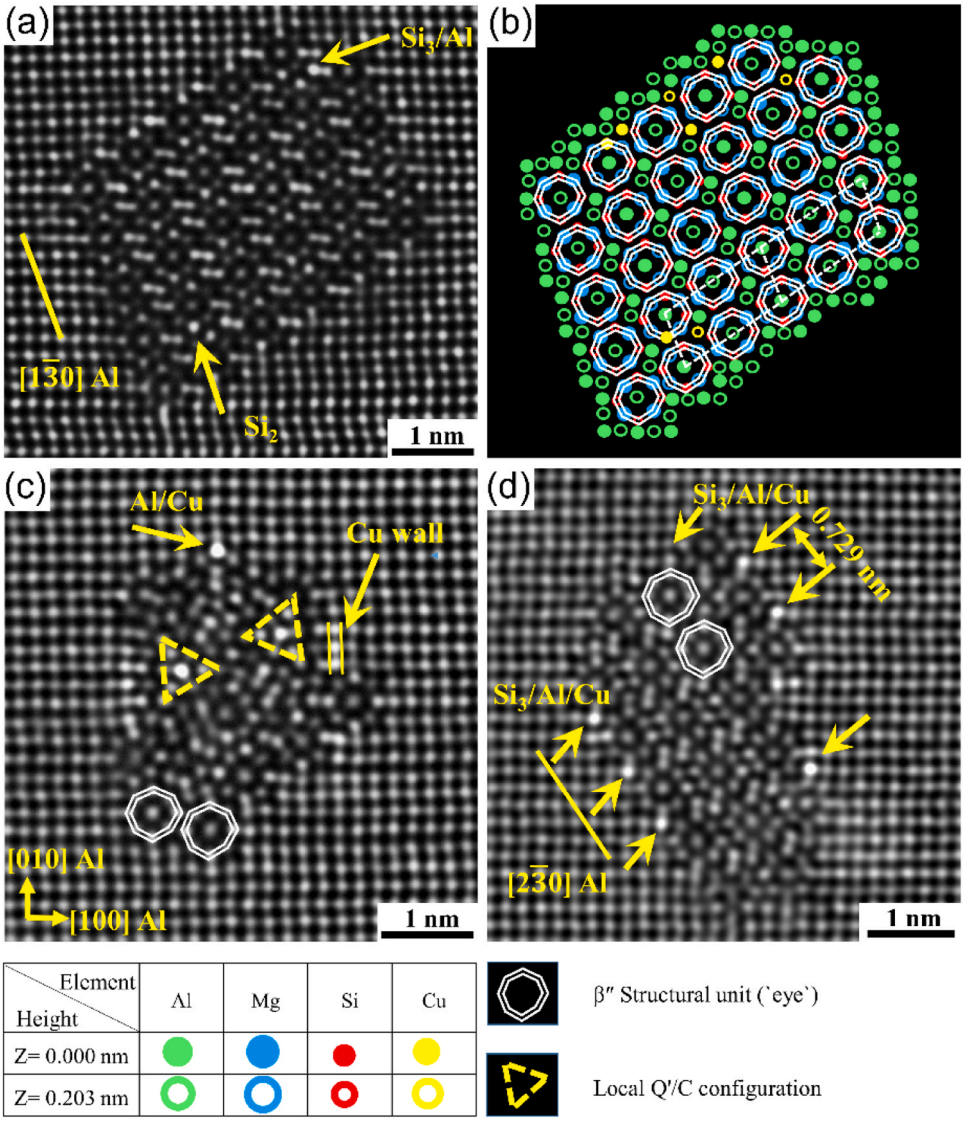

Fig. 7. High-resolution HAADF-STEM images (a, c, d) of several precipitates in sample A1; (b) reconstructed atomic structure of the precipitate shown in (a).

4. Discussion

The key finding in this study is that improved corrosion resistance can be achieved in the AA6082 alloy containing 0.05 wt% Cu by controlling the Zn-content. Furthermore, it is also found that minor additions of Zn and Cu can significantly affect the crystal structure of hardening precipitates produced during aging. Critical insights into the different behavior of Cu and Zn segregating along GBs and the tendency to alter precipitate crystal structures are obtained in this study. To the best of our knowledge, the present work is the first detailed investigation of the combined effects of both Cu and Zn present in low concentrations in the industrially important AA6082 alloy. Our findings provide evidence of the possibility to improve the resistance to IGC in recycled 6xxx Al alloys by balancing levels of Zn and Cu without compromising the hardness (see Fig. 3). In the following, we shall discuss the effect of varying Zn content on the microstructure and IGC of the peak aged AA6082 alloy containing 0.05 wt% Cu.

4.1. Effect of Zn on the microstructure

As shown in Figs. 1, 2, and 4, except for the somewhat different average grain size near the immediate surface, there are no apparent differences in the microstructure of samples A1 to A4 studied by optical microscopy, SEM/EBSD, and conventional TEM. Most importantly, all the studied samples demonstrate similar frequencies of needle-shaped β″ and rod-shaped β′ precipitates. Based on HAADF-STEM, it can be suggested that small additions of Cu and Zn do not alter the precipitation sequence typical of Al-Mg-Si alloys, but introduce different sub-unit structures into β″ precipitates, e.g., U2, Q/Q′, and β'_{Cu}.

Additionally, in sample A1, Cu atoms enter the crystal structure of the β″ precipitates and preferentially replace or partially occupy the Si_3/Al atomic columns [53,54], see Fig. 7a,d. For precipitates with more disordered structures, at least two of the following substructures coexist within individual precipitates: β″, β'_{Cu} and Q′/C, see Fig. 7c. These findings demonstrate how very low Cu content expected to be found in recycled alloys can influence the precipitate structures in Al-Mg-Si alloys in the peak-aged condition. Sunde et al. [55,56] investigated the influence of small Cu additions on the crystal structure of Al-Mg-Si precipitates formed under different aging conditions. These authors reported that the majority of the precipitates in 6082-type alloys with 0.03 and 0.09 wt% Cu in the peak aged condition were pure β″. In the 0.03 wt% Cu alloy, Cu atoms did not affect the crystal structure of β″, showing only slight enrichment of specific atomic columns in the β″ structure or residing at the β″/Al interface. However, an alloy with 0.09 wt% Cu showed the presence of individual β'_{Cu} sub-units in the β″ precipitates. Therefore, our findings demonstrate that 0.05 wt% Cu can

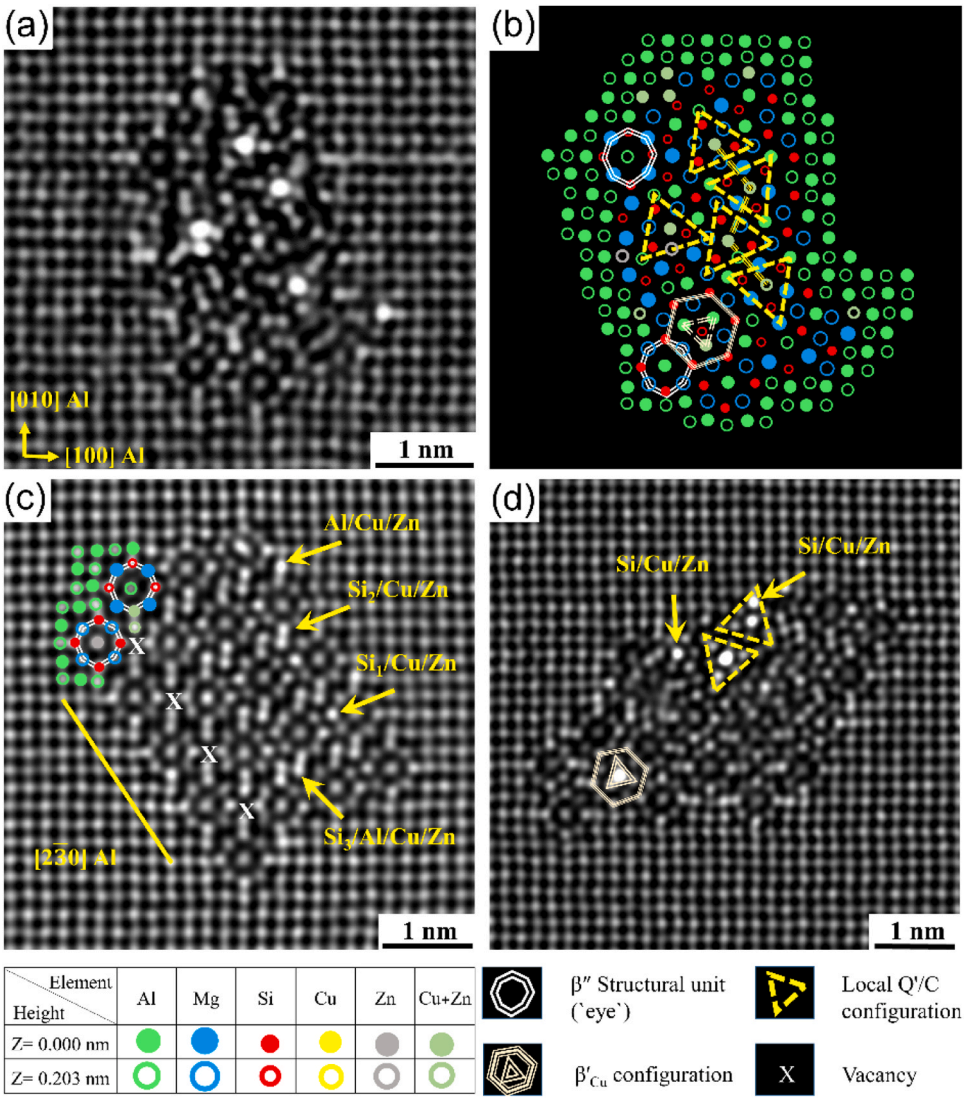

Fig. 8. High-resolution HAADF-STEM images (a, c, d) of several precipitates in sample A4; (b) reconstructed atomic structure of the precipitate shown in (a).

noticeably influence the precipitate structure of the main hardening precipitates in Al-Mg-Si alloys, introducing different unit structures such as β′$_{Cu}$ and Q′/C inside the β″ structure.

In sample A4 containing 0.06 wt% Zn, changes in the precipitate structure and an increase in the frequency of disordered precipitates are observed, such as those shown in Fig. 8a,d. The β″ precipitates are still the main hardening precipitates, but the frequency of disordered structures is significantly greater than in sample A1. No precipitates such as η-MgZn$_2$ or their precursors typical of the Al-Mg-Zn system are found in sample A4. This suggests that such low concentrations of Zn can noticeably modify the precipitate structure of the β″ phase, without affecting the precipitation sequences through introducing phases observed in Al-Mg-Zn alloys.

4.2. Susceptibility to intergranular corrosion

The studied samples show clear differences in the chemical compositions of GB particles and GB films as a result of different small Zn concentrations in the studied samples. Based on our STEM observations, the key differences between samples A1 and A4 are schematically illustrated in Fig. 12. This figure shows the presence of Cu-rich films and two different types of particles along GBs (β and Q/Q′) in sample A1 and the presence of Cu/Zn-rich films and two types of particles at the GBs (Zn-free Q/Q′ and Zn-containing Q/Q′) in sample A4. The presence of Cu-rich films along GBs as well as the Q/Q′ particles is thought to be the driving force for IGC in sample A1. Cu, being nobler than Al, Mg, and Si, shifts the corrosion potential of the GBs toward a more positive value, leading to the dissolution of adjacent area. Moreover, the presence of β (Mg$_2$Si) GB particles will additionally promote IGC as these particles will act as anodes when exposed to an acidified solution [1,9,57]. The selective dissolution of Mg from β (Mg$_2$Si) particles leaves Si-rich remnants [58,59], which will further act as active cathodes supporting the cathodic sites until the oxidation of Si occurs [15,58,60,61]. This explains the relatively low IGC resistance of sample A1, where the Cu-rich GB films in addition to the Q/Q′ phases act as cathodes and the area adjacent to the GBs, together with β particles, act as anodes, resulting in the dissolution of PFZs and GBs [17,62–64].

On the other hand, the presence of 0.06 wt% Zn in sample A4 changes the chemical composition of GBs, where Zn-free Q/Q′ particles and Zn-containing Q/Q′ particles, as well as Cu- and Zn-rich films are observed along the GBs (Fig. 6). Based on the STEM observations, it is suggested that Zn is located at or near particle/matrix interfaces, as well as inside the crystal structure, and thus may affect the electrochemical potentials of these particles. Any presence of Zn at or near GBs can reduce the detrimental effect of Cu by balancing the difference in electrochemical potentials between GBs, GB particles, and PFZs. The results

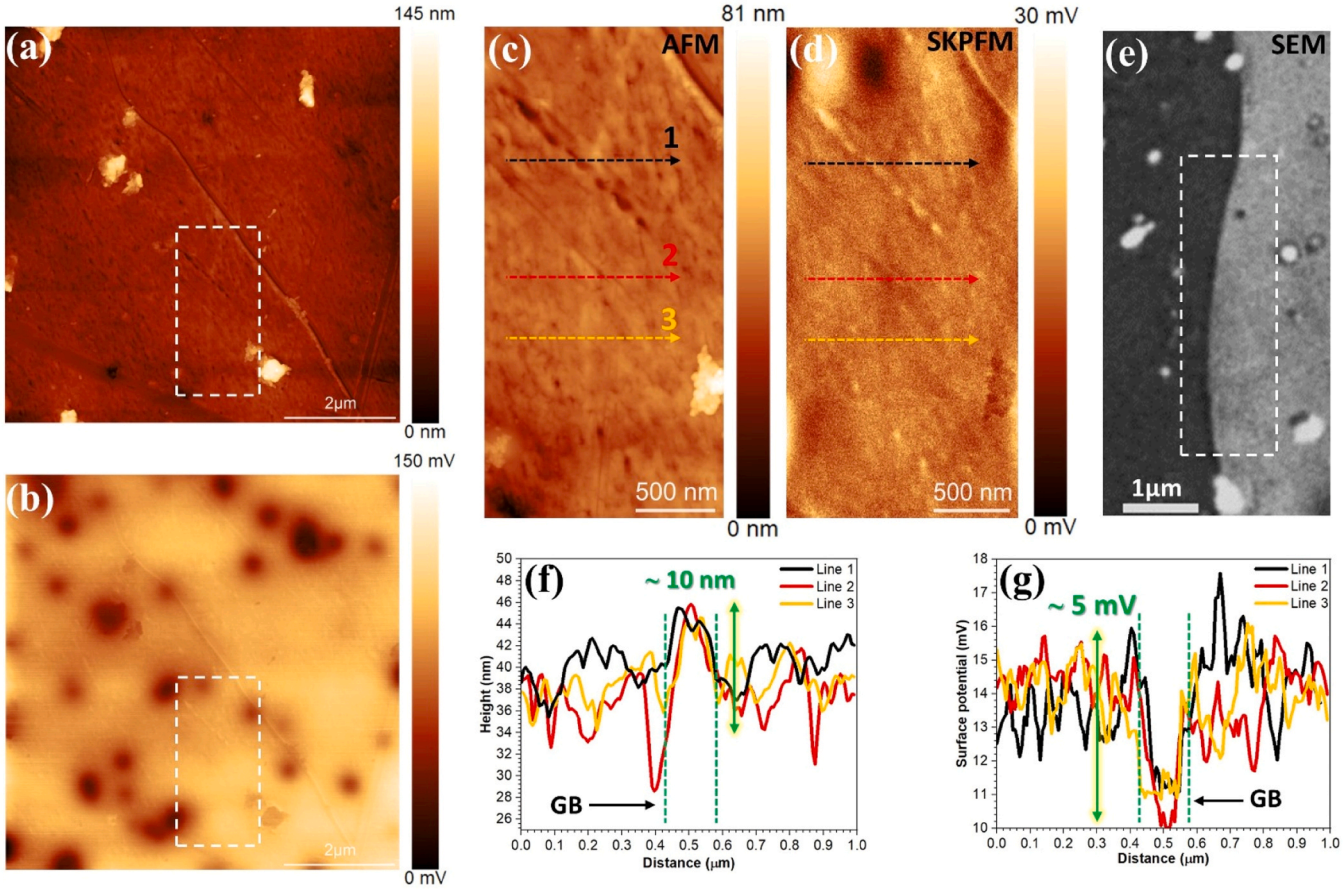

Fig. 9. (a, b) low-magnification AFM and SKPFM images where large intermetallic particles are seen as dark features; (c, d) high-magnification AFM and SKPFM images of the GB region; (e) SEM/BSE image of a region containing a GB additionally analyzed by AFM/SKPFM in (c, d); (f) topography and (g) surface-potential profiles along three dashed lines shown in (c, d). Dashed lines in (g) indicate regions with reduced surface potentials.

indicate that this reduction can be achieved when Zn is added in concentrations close to those of Cu, thus minimizing the differences in electrochemical potentials between PFZs and the matrix, and therefore resulting in better IGC resistance of samples A2, A3, and A4 compared to that of sample A1. A clear positive effect of the increased Zn concentration on reducing the extent of IGC N_C and the maximum penetration depth Z_C is observed in Fig. 11.

Therefore, it can be concluded that Zn can offset the negative effect of Cu on the IGC resistance of the AA6082 alloy in the peak-aged condition. The effect is evident when Zn is added with concentrations close to those of Cu (0.06 wt% Zn and 0.05 wt% Cu). Our results are different from those reported by Guo et al. [65], who found that the resistance to IGC decreased as the Zn content in Al-Mg-Si-Cu-Zn alloys increased from 0 to 1 wt%. It is suggested that the presence of 1 wt% Zn in these alloys resulted in a higher Zn concentration than necessary to mitigate the detrimental effects of 0.2 wt% Cu, leading to different corrosion potentials between PFZs and grain interiors. It should be noted that adding only Zn or only Cu to Al-Mg-Si alloys, in general, negatively influences the IGC resistance and that the negative effect is often proportional to concentrations of Cu and Zn [1,64,66–68].

However, in some cases, a higher Cu concentration at GBs can negatively influence the IGC resistance due to an unbalanced electrochemical effect. The lower surface potential observed in the lower part of Fig. 9g can be considered a clear example of the compositional heterogeneity at the GB due to unbalanced concentrations of Cu and Zn. The low magnitude of the surface potential and/or surface charge difference between the GB and its adjacent area could originate due to the presence of a native oxide film in the aluminum alloy (γ-Al_2O_3 with a considerable band gap energy) [69]. Consequently, this native oxide film could considerably affect the total surface potential and/or surface charge signal, which causes less tendency to establish a significant electrostatic force between metal/oxide and tip-apex in the surface-sensitive SKPFM analysis (Figure S4) [70].

5. Conclusions

This study demonstrates an important strategy for improving the IGC resistance of peak-aged Al-Mg-Si alloys with 0.05 wt% Cu by adding a similar (0.06 wt%) concentration of Zn. The results indicate that the underlying mechanisms are minimizing differences in electrochemical potentials between grain boundary regions, grain boundary particles, precipitate-free zones, and the matrix. Furthermore, this work demonstrates how minor additions of Zn and/or Cu can influence the crystal structure of Al-Mg-Si precipitates after peak-aging. The following conclusions are drawn:

1. Sample A1 containing 0.05 wt% Cu is found to be highly susceptible to IGC. The driving force for the IGC is the formation of Cu-rich films in addition to the presence of Q/Q′ and β particles along GBs.
2. The IGC resistance in the Al-Mg-Si alloys with 0.05 wt% Cu can be controlled by adding an appropriate amount of Zn. The addition of 0.06 wt% Zn noticeably suppresses the IGC in the alloys studied in this work. The presence of Zn in Q′/Q particles and at GBs, along with the Cu-rich films, reduce the driving force for IGC by reducing the difference in the electrochemical potential between cathodic sites and anodic sites.
3. The addition of 0.05 wt% Cu and 0.06 wt% Zn to Al-Mg-Si alloys can significantly influence the precipitate crystal structures. A high

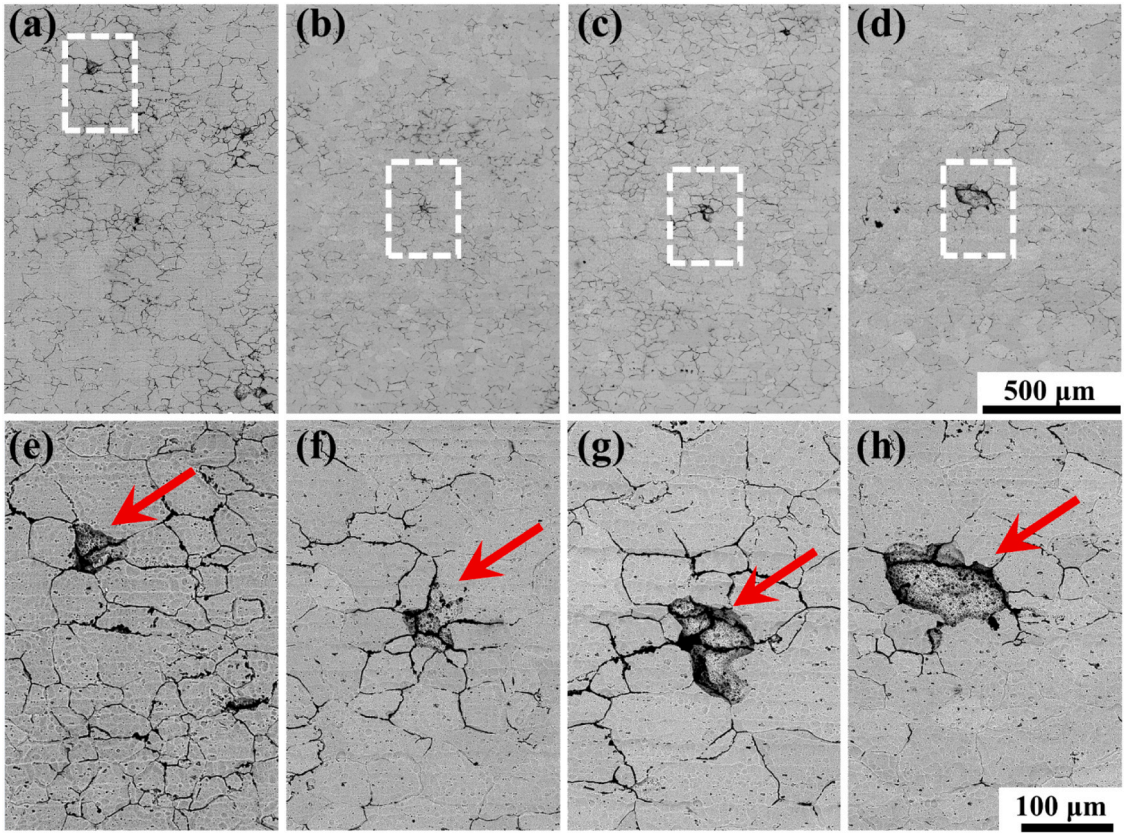

Fig. 10. SEM/BSE images of the surface of specimens subjected to the IGC tests: (a) sample A1, (b) sample A2, (c) sample A3, and (d) sample A4; (e, f, g, and h) higher magnification images of the framed areas in (a, b, c, and d). Arrows in (e-h) show cavities inside the IGC network as a result of grains which have fallen out.

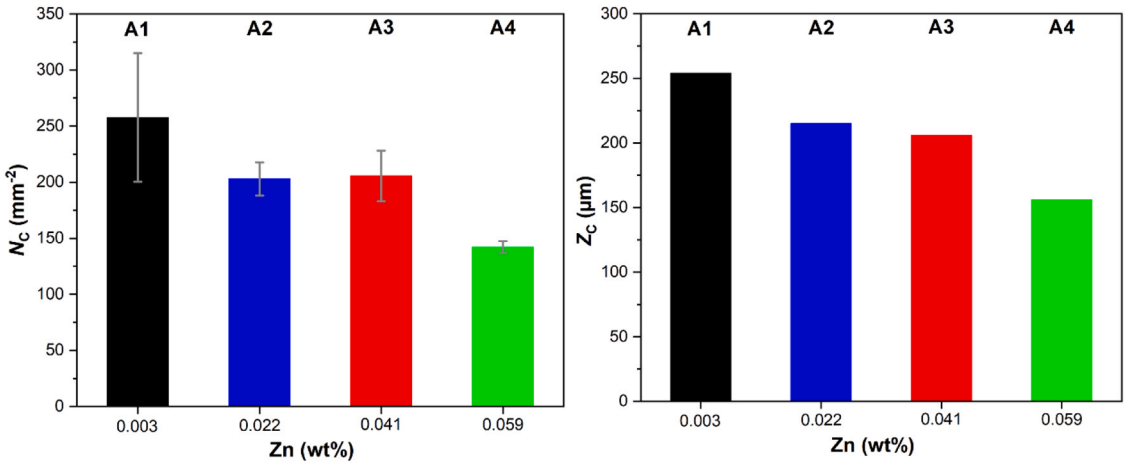

Fig. 11. Parameters of IGC in the samples with different concentrations of Zn: (a) number of corroded boundaries per unit area N_C calculated based on SEM examinations of the ED-TD plane; (b) maximum depth of the IGC attack Z_C measured in the ED-ND plane.

frequency of the precipitates is found to be disordered. Two different Cu-containing sub-units (Q'/C and β'_{Cu}) are detected in the crystal structure of β'' precipitates.

4. Cu enters the precipitates within their established unit structures, e. g. Q/Q' and/or β'_{Cu} unit structures. However, Zn does not show a tendency to occupy specific columns in the precipitate structure.

CRediT authorship contribution statement

Emad Hasan Bartawi: Writing – review & editing, Writing – original draft, Methodology, Investigation, Formal analysis, Conceptualization. **Calin Marioara:** Writing – review & editing, Investigation, Formal analysis. **Ghada Shaban:** Writing – review & editing, Investigation, Formal analysis. **Ehsan Rahimi:** Writing – review & editing, Formal analysis. **Oleg Mishin:** Writing – review & editing, Investigation, Formal analysis. **Jonas Sunde:** Writing – review & editing. **Yaiza Gonzalez Garcia:** Writing – review & editing. **Randi Holmestad:** Writing – review & editing. **Rajan Ambat:** Writing – review & editing, Methodology, Funding acquisition, Conceptualization.

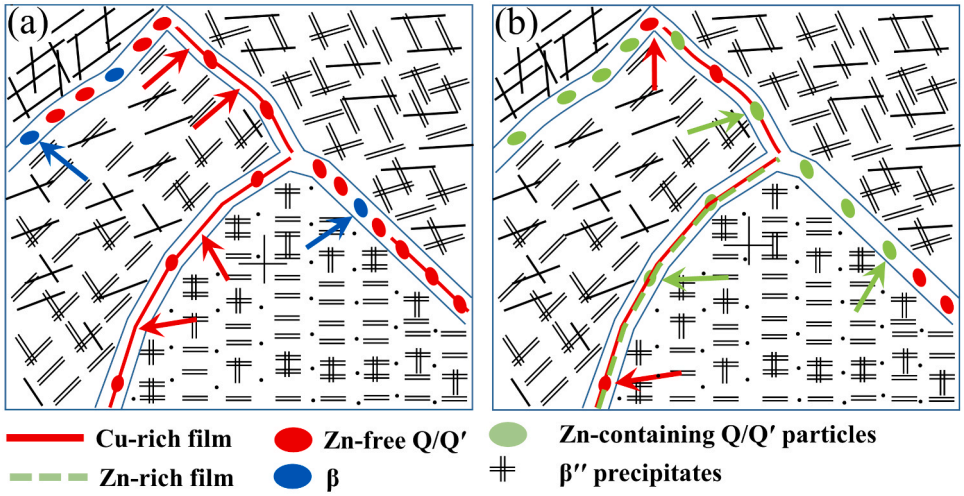

Fig. 12. Schematic illustration of GBs and Al matrix with fine precipitates in the samples (a) with 0.05 wt% Cu and (b) with 0.05 wt% Cu and 0.06 wt% Zn. Cu and Zn-rich films along the GBs are represented by solid red and dashed green lines, respectively. Zn-free Q/Q′ particles are shown in red, β particles are shown in blue, and Zn-containing Q/Q′ particles are shown in green, while β″ and β′ precipitates in the matrix are shown as black lines. The black dots in one of the grains represent cross-sections of hardening precipitates assuming that this grain is oriented along a ⟨001⟩ zone axis.

Declaration of Competing Interest

The authors declare that they have no known competing financial interests or personal relationships that could have appeared to influence the work reported in this paper.

Data availability

Data will be made available on request.

Acknowledgements

The authors would like to thank Hydro Aluminium, Norway, for providing material. The authors also would like to thank Dr. J. Kling from DTU Nanolab and Dr. Ruben Bjørge from SINTEF Industry for their assistance during STEM experiments. EHB and RA acknowledge funding from the Independent Research Fund Denmark (grant number 9041-00240A). Also, this project has received funding from the European Union's Horizon 2020 research and innovation programme under grant agreement No 823717-ESTEEM3. The HR-STEM work was conducted on the NORTEM (Norwegian Research Council project number: 197405) infrastructure at the TEM Gemini Centre, Trondheim, Norway.

Appendix A. Supporting information

Supplementary data associated with this article can be found in the online version at doi:10.1016/j.corsci.2024.112227.

References

[1] J.R. Davis, Corrosion of Aluminum and Aluminum Alloys, ASM international, 1999.
[2] J. Hirsch, Recent development in aluminium for automotive applications, Trans. Nonferrous Met. Soc. China 24 (2014) 1995–2002.
[3] C. Poletti, M. Rodriguez-Hortalá, M. Hauser, C. Sommitsch, Microstructure development in hot deformed AA6082, Mater. Sci. Eng. A 528 (2011) 2423–2430.
[4] J. Hu, W. Zhang, D. Fu, J. Teng, H. Zhang, Improvement of the mechanical properties of Al-Mg-Si alloys with nano-scale precipitates after repetitive continuous extrusion forming and T8 tempering, J. Mater. Res. Technol. 8 (2019) 5950–5960.
[5] A. Serizawa, T. Sato, M.K. Miller, Effect of cold rolling on the formation and distribution of nanoclusters during pre-aging in an Al–Mg–Si alloy, Mater. Sci. Eng. A 561 (2013) 492–497.
[6] F. Serradj, R. Guemini, H. Farh, K. Djemmal, Study of mechanical and electrical properties of AlMgSi alloys, Ann. Chim. (2010) 59–69.
[7] T. Saito, S. Wenner, E. Osmundsen, C.D. Marioara, S.J. Andersen, J. Røyset, W. Lefebvre, R. Holmestad, The effect of Zn on precipitation in Al-Mg-Si alloys, Philos. Mag. 94 (2014) 2410–2425.
[8] C.D. Marioara, A. Lervik, J. Grønvold, O. Lunder, S. Wenner, T. Furu, R. Holmestad, The correlation between intergranular corrosion resistance and copper content in the precipitate microstructure in an AA6005A alloy, Metall. Mater. Trans. A 49 (2018) 5146–5156.
[9] X. Zhang, X. Zhou, J.O. Nilsson, Corrosion behaviour of AA6082 Al-Mg-Si alloy extrusion: the influence of quench cooling rate, Corros. Sci. 150 (2019) 100–109.
[10] E.H. Bartawi, O.V. Mishin, G. Shaban, J.H. Nordlien, R. Ambat, Electron microscopy analysis of grain boundaries and intergranular corrosion in aged Al-Mg-Si alloy doped with 0.05 wt% Cu, Corros. Sci. 209 (2022) 110758.
[11] A. Lervik, S. Wenner, O. Lunder, C.D. Marioara, R. Holmestad, Grain boundary structures and their correlation with intergranular corrosion in an extruded Al-Mg-Si-Cu alloy, Mater. Charact. 170 (2020) 110695.
[12] X. Zhang, X. Zhou, J.O. Nilsson, Z. Dong, C. Cai, Corrosion behaviour of AA6082 Al-Mg-Si alloy extrusion: recrystallized and non-recrystallized structures, Corros. Sci. 144 (2018) 163–171.
[13] D.J. Chakrabarti, D.E. Laughlin, Phase relations and precipitation in Al–Mg–Si alloys with Cu additions, Prog. Mater. Sci. 49 (2004) 389–410.
[14] W. Yang, S. Ji, Z. Li, M. Wang, Grain boundary precipitation induced by grain crystallographic misorientations in an extruded Al-Mg-Si-Cu alloy, J. Alloy. Compd. 624 (2015) 27–30.
[15] G. Svenningsen, J.E. Lein, A. Bjørgum, J.H. Nordlien, Y. Yu, K. Nisancioglu, Effect of low copper content and heat treatment on intergranular corrosion of model AlMgSi alloys, Corros. Sci. 48 (2006) 226–242.
[16] C. Schnatterer, D. Zander, Influence of the grain boundary chemistry on the intergranular corrosion mechanisms of a high-strength Al-Mg-Si alloy, Surf. Interface Anal. 48 (2016) 750–754.
[17] G. Svenningsen, M.H. Larsen, J.C. Walmsley, J.H. Nordlien, K. Nisancioglu, Effect of artificial aging on intergranular corrosion of extruded AlMgSi alloy with small Cu content, Corros. Sci. 48 (2006) 1528–1543.
[18] G. Svenningsen, M.H. Larsen, J.H. Nordlien, K. Nisancioglu, Effect of thermomechanical history on intergranular corrosion of extruded AlMgSi(Cu) model alloy, Corros. Sci. 48 (2006) 3969–3987.
[19] Z. Wang, H. Li, F. Miao, W. Sun, B. Fang, R. Song, Z. Zheng, Improving the intergranular corrosion resistance of Al–Mg–Si–Cu alloys without strength loss by a two-step aging treatment, Mater. Sci. Eng. A 590 (2014) 267–273.
[20] H. Hug, Ueber den einflußgeringer schwermetallgehalte auf die korrosionsbeständigkeit von Al-Mg-Si Legierungen, Aluminium 23 (1941) 33.
[21] K. Nisancioglu, Ø. Strandmyr, Corrosion of AlMgSi alloys with Cu additions: the effect of Cu content up to 0.9 wt percent, Report no, STF34 A78052, SINTEF, Trondheim, Norw. (1978).
[22] E.H. Bartawi, O.V. Mishin, G. Shaban, F. Grumsen, J.H. Nordlien, R. Ambat, The effect of trace level copper content on intergranular corrosion of extruded AA6082-T6 alloys, Mater. Chem. Phys. (2023) 128303.
[23] J.F. Nie, Physical Metallurgy of Light Alloys. Fifth Edit, Elsevier, 2014.
[24] S.K. Kairy, P.A. Rometsch, K. Diao, J.F. Nie, C.H.J. Davies, N. Birbilis, Exploring the electrochemistry of 6xxx series aluminium alloys as a function of Si to Mg ratio, Cu content, ageing conditions and microstructure, Electrochim. Acta 190 (2016) 92–103.
[25] T. Saito, E.A. Mørtsell, S. Wenner, C.D. Marioara, S.J. Andersen, J. Friis, K. Matsuda, R. Holmestad, Atomic structures of precipitates in Al–Mg–Si alloys with small additions of other elements, Adv. Eng. Mater. 20 (2018) 1800125.

[26] G.A. Edwards, K. Stiller, G.L. Dunlop, M.J. Couper, The precipitation sequence in Al–Mg–Si alloys, Acta Mater. 46 (1998) 3893–3904.
[27] W.F. Miao, D.E. Laughlin, Effects of Cu content and preaging on precipitation characteristics in aluminum alloy 6022, Metall. Mater. Trans. A 31 (2000) 361–371.
[28] M. Murayama, K. Hono, W. Miao, D.E. Laughlin, The effect of Cu additions on the precipitation kinetics in an Al-Mg-Si alloy with excess Si, Metall. Mater. Trans. A 32 (2001) 239–246.
[29] Z. Jia, L. Ding, L. Cao, R. Sanders, S. Li, Q. Liu, The influence of composition on the clustering and precipitation behavior of Al-Mg-Si-Cu alloys, Metall. Mater. Trans. A 48 (2017) 459–473.
[30] C. Cayron, L. Sagalowicz, L. Sagalowicz, P.A. Buffat, Structural phase transition in Al-Cu-Mg-Si alloys by transmission electron microscopy study on an Al-4 wt% Cu-1 wt% Mg-Ag alloy reinforced by SiC particles, Philos. Mag. A 79 (1999) 2833–2851.
[31] C.D. Marioara, S.J. Andersen, T.N. Stene, H. Hasting, J. Walmsley, A.T.J. Van Helvoort, R. Holmestad, The effect of Cu on precipitation in Al-Mg-Si alloys, Philos. Mag. 87 (2007) 3385–3413.
[32] C.D. Marioara, S.J. Andersen, J. Røyset, O. Reiso, S. Gulbrandsen-Dahl, T. E. Nicolaisen, I.E. Opheim, J.F. Helgaker, R. Holmestad, Improving thermal stability in Cu-containing Al-Mg-Si alloys by precipitate optimization, Metall. Mater. Trans. A 45 (2014) 2938–2949.
[33] T. Saito, C.D. Marioara, S.J. Andersen, W. Lefebvre, R. Holmestad, Aberration-corrected HAADF-STEM investigations of precipitate structures in Al-Mg-Si alloys with low Cu additions, Philos. Mag. 94 (2014) 520–531.
[34] K. Matsuda, S. Ikeno, Y. Uetani, T. Sato, Metastable phases in an Al-Mg-Si alloy containing copper, Metall. Mater. Trans. A 32 (2001) 1293–1299.
[35] L. Arnberg, B. Aurivillius, E. Wahlström, G. Malmros, J. Sjöblom, T.G. Strand, V. F. Sukhoverkhov, The crystal structure of Al(x)Cu2Mg(12-x)Si7, (h-AlCuMgSi), Acta Chem. Scand. 34 (1980) 1–5.
[36] X. Xu, W. Zhu, M. Yuan, C. Liang, Y. Deng, The effect of Zn content on the microstructure and mechanical properties of the Al-mg-Si alloy, Mater. Charact. 198 (2023) 112714.
[37] S. Zhu, Z. Li, L. Yan, X. Li, S. Huang, H. Yan, Y. Zhang, B. Xiong, Natural aging behavior in pre-aged Al–Mg–Si–Cu alloys with and without Zn addition, J. Alloy. Compd. 773 (2019) 496–502.
[38] X.P. Ding, H. Cui, J.X. Zhang, H.X. Li, M.X. Guo, Z. Lin, L.Z. Zhuang, J.S. Zhang, The effect of Zn on the age hardening response in an Al-Mg-Si alloy, Mater. Des. 65 (2015) 1229–1235.
[39] M.X. Guo, Y.D. Zhang, G.J. Li, S.B. Jin, G. Sha, J.S. Zhang, L.Z. Zhuang, E. J. Lavernia, Solute clustering in Al-Mg-Si-Cu-(Zn) alloys during aging, J. Alloy. Compd. 774 (2019) 347–363.
[40] W. Yang, W. Shen, R. Zhang, K. Cao, J. Zhang, L. Liu, Enhanced age-hardening by synergistic strengthening from MgSi and MgZn precipitates in Al-Mg-Si alloy with Zn addition, Mater. Charact. 169 (2020) 110579.
[41] T. Saito, F.J.H. Ehlers, W. Lefebvre, D. Hernandez-Maldonado, R. Bjørge, C. D. Marioara, S.J. Andersen, R. Holmestad, HAADF-STEM and DFT investigations of the Zn-containing β'' phase in Al-Mg-Si alloys, Acta Mater. 78 (2014) 245–253.
[42] S. Chi, Y. Deng, X. Xu, X. Guo, Influence of minor Zn addition on precipitation behavior and intergranular corrosion properties of Al-Mg-Si alloy, Materials 13 (2020) 650.
[43] K. Yamaguchi, K. Tohma, Effect of Zn addition on intergranular corrosion resistance of Al-Mg-Si-Cu alloys, : Proc. 6th Int. Conf. Alum. Alloy. Toyohashi (1998) 1657–1662.
[44] Z. Jin, C. Cai, T. Hashimoto, Y. Yuan, D.H. Kang, J. Hunter, X. Zhou, Alkaline etching and desmutting of aluminium alloy: the behaviour of Mg2Si particles, J. Alloy. Compd. 842 (2020) 155834.
[45] E.N. ISO, Corrosion of metals and alloys. Determination of resistance to intergranular corrosion of solution heat-treatable aluminium alloys, Br. Stand. Inst. (2005).
[46] S. Kumari, S. Wenner, J.C. Walmsley, O. Lunder, K. Nisancioglu, Progress in understanding initiation of intergranular corrosion on AA6005 aluminum alloy with low copper content, J. Electrochem. Soc. 166 (2019) C3114–C3123.
[47] S.J. Andersen, H.W. Zandbergen, J. Jansen, C. Træholt, U. Tundal, O. Reiso, The crystal structure of the β″ phase in Al-Mg-Si Alloys, Acta Mater. 46 (1998) 3283–3298.
[48] S.J. Andersen, C.D. Marioara, R. Vissers, A. Frøseth, H.W. Zandbergen, The structural relation between precipitates in Al–Mg–Si alloys, the Al-matrix and diamond silicon, with emphasis on the trigonal phase U1-MgAl2Si2, Mater. Sci. Eng. A 444 (2007) 157–169.
[49] S.J. Andersen, C.D. Marioara, A. Frøseth, R. Vissers, H.W. Zandbergen, Crystal structure of the orthorhombic U2-Al4Mg4 Si4 precipitate in the Al-Mg-Si alloy system and its relation to the β′ and β″ phases, Mater. Sci. Eng. A 390 (2005) 127–138.
[50] H. Tvedt, C.D. Marioara, E. Thronsen, C. Hell, S.J. Andersen, R. Holmestad, AutomAl 6000: Semi-automatic structural labelling of HAADF-STEM images of precipitates in Al–Mg–Si(–Cu) alloys, Ultramicroscopy 236 (2022) 113493.
[51] E.H. Bartawi, C.D. Marioara, G. Shaban, C. Hatzoglou, R. Holmestad, R. Ambat, Atomic Structure of Hardening Precipitates in Al−Mg−Si Alloys: Influence of Minor Additions of Cu and Zn, (n.d.).
[52] S.J. Andersen, C.D. Marioara, J. Friis, R. Bjørge, Q. Du, I.G. Ringdalen, S. Wenner, E.A. Mørtsell, R. Holmestad, T. Saito, J. Røyset, O. Reiso, Directionality and column arrangement principles of precipitates in Al-Mg-Si-(Cu) and Al-Mg-Cu linked to line defect in Al, Mater. Sci. Forum 877 (2017) 461–470.
[53] R. Vissers, M.A. van Huis, J. Jansen, H.W. Zandbergen, C.D. Marioara, S. J. Andersen, The crystal structure of the β′ phase in Al–Mg–Si alloys, Acta Mater. 55 (2007) 3815–3823.
[54] H.S. Hasting, A.G. Frøseth, S.J. Andersen, R. Vissers, J.C. Walmsley, C.D. Marioara, F. Danoix, W. Lefebvre, R. Holmestad, Composition of B″ precipitates in Al-Mg-Si alloys by atom probe tomography and first principles calculations, J. Appl. Phys. 106 (2009) 12, 106.
[55] J.K. Sunde, C.D. Marioara, R. Holmestad, The effect of low Cu additions on precipitate crystal structures in overaged Al-Mg-Si(-Cu) alloys, Mater. Charact. 160 (2020) 110087.
[56] J.K. Sunde, C.D. Marioara, A.T.J. van Helvoort, R. Holmestad, The evolution of precipitate crystal structures in an Al-Mg-Si(-Cu) alloy studied by a combined HAADF-STEM and SPED approach, Mater. Charact. 142 (2018) 458–469.
[57] R.K. Gupta, N.L. Sukiman, K.M. Fleming, M.A. Gibson, N. Birbilis, Electrochemical behavior and localized corrosion associated with Mg2Si particles in Al and Mg alloys, ECS Electrochem. Lett. 1 (2012) 1–4.
[58] F. Eckermann, T. Suter, P.J. Uggowitzer, A. Afseth, P. Schmutz, The influence of MgSi particle reactivity and dissolution processes on corrosion in Al–Mg–Si alloys, Electrochim. Acta 54 (2008) 844–855.
[59] K.M. Fleming, A. Zhu, J.R. Scully, Corrosion of AA6061 brazed with an Al-Si alloy: effects of Si on metallurgical and corrosion behavior, Corrosion 68 (2012) 1126–1145.
[60] F.L. Zeng, Z.L. Wei, J.F. Li, C.X. Li, X. Tan, Z. Zhang, Z.Q. Zheng, Corrosion mechanism associated with Mg2Si and Si particles in Al–Mg–Si alloys, Trans. Nonferrous Met. Soc. China 21 (2011) 2559–2567.
[61] L.I. Chaoxing, L.I. Jinfeng, B. Nick, J.I.A. Zhiqiang, Z. Ziqiao, Synergetic effect of Mg2Si and Si particles on intergranular corrosion of Al-Mg-Si alloys through multi-electrode coupling system, J. Chin. Soc. Corros. Prot. 30 (2010) 107–113.
[62] S.K. Kairy, T. Alam, P.A. Rometsch, C.H.J. Davies, R. Banerjee, N. Birbilis, Understanding the origins of intergranular corrosion in copper-containing Al-Mg-Si alloys, Metall. Mater. Trans. A Phys. Metall. Mater. Sci. 47 (2016) 985–989.
[63] M.H. Larsen, J.C. Walmsley, O. Lunder, R.H. Mathiesen, K. Nisancioglu, Intergranular corrosion of copper-containing AA6xxx AlMgSi aluminum alloys, J. Electrochem. Soc. 155 (2008) C550.
[64] Y. Zou, Q. Liu, Z. Jia, Y. Xing, L. Ding, X. Wang, The intergranular corrosion behavior of 6000-series alloys with different Mg/Si and Cu content, Appl. Surf. Sci. 405 (2017) 489–496.
[65] M.X. Guo, J.Q. Du, C.H. Zheng, J.S. Zhang, L.Z. Zhuang, Influence of Zn contents on precipitation and corrosion of Al-Mg-Si-Cu-Zn alloys for automotive applications, J. Alloy. Compd. 778 (2019) 256–270.
[66] X. Xu, Y. Deng, Q. Pan, X. Guo, Enhancing the intergranular corrosion resistance of the Al–Mg–Si alloy with low Zn content by the interrupted aging treatment, Metall. Mater. Trans. A 52 (2021) 4907–4921.
[67] M.H. Larsen, J.C. Walmsley, O. Lunder, K. Nisancioglu, Significance of low copper content on grain boundary nanostructure and intergranular corrosion of AlMgSi (Cu) model alloys, in: Mater. Sci. Forum, Trans Tech Publications Ltd, 2006, pp. 667–672.
[68] H. Zhan, J.M.C. Mol, F. Hannour, L. Zhuang, H. Terryn, J.H.W. De Wit, The influence of copper content on intergranular corrosion of model AlMgSi(Cu) alloys, Mater. Corros. 59 (2008) 670–675.
[69] L. Nguyen, T. Hashimoto, D.N. Zakharov, E.A. Stach, A.P. Rooney, B. Berkels, G. E. Thompson, S.J. Haigh, T.L. Burnett, Atomic-scale insights into the oxidation of aluminum, ACS Appl. Mater. Interfaces 10 (2018) 2230–2235.
[70] E. Rahimi, A. Imani, M. Lekka, F. Andreatta, Y. Gonzalez-Garcia, J.M.C. Mol, E. Asselin, L. Fedrizzi, Morphological and surface potential characterization of protein nanobiofilm formation on magnesium alloy oxide: their role in biodegradation, Langmuir 38 (2022) 10854–10866.